Rotational modulation and flares on RS Canum Venaticorum and BY Draconis stars

XI. Ultraviolet spectral images of AR Lacertae in September 1985 [*]

J. E. Neff [1, **], **F. M. Walter** [2, **], **M. Rodonò** [3, **], and **J. L. Linsky** [1, 4]

[1] Joint Institute for Laboratory Astrophysics, University of Colorado, Boulder, CO 80309-0440, USA
[2] Center for Astrophysics and Space Astronomy, University of Colorado, Boulder, CO 80309-0391, USA
[3] Istituto di Astronomia, University of Catania and Osservatorio Astrofisico, Viale A. Doria 6, I-95125 Catania, Italy
[4] Quantum Physics Division, National Institute of Standards and Technology

Summary. Using a series of high-resolution ultraviolet spectra, we have derived a series of images of the chromosphere of AR Lacertae. In September 1985, neither star in this system was uniformly bright. The trailing hemisphere of the K0 IV star was globally brighter than the leading hemisphere. The position, size, and surface flux of three distinct plage regions on the K star were measured with our spectral imaging procedure. We interpret the factor of 3 variability in total emission from the G2 IV star as due to a large chromospherically inactive region on its surface. We were able to constrain the position, size, and surface flux of a flaring region on the G star and to measure a significant redshift and broadening of the line emission from the flaring region. We used the rotational modulation of the integrated low-resolution line fluxes to determine the far-ultraviolet spectra of the global K and G stars and of the plage and flare regions alone.

Key words: stars: atmospheres of – stars: binary: spectroscopic – stars: chromospheres of – stars: AR Lacertae

1. Introduction

The presence of emission lines in the ultraviolet spectra of late-type stars indicates that hot, thin plasma – analogous to the solar chromosphere and transition region – must overlay their photospheres. Bright line emission from the solar chromosphere arises primarily in magnetically-confined plage regions, and the physical conditions outside of the plages are very different from those inside of them. Spatial resolution of the solar atmosphere permits us to determine the spectra and thus the physical properties of both plage and non-plage regions separately. All other stars, unfortunately, appear as unresolved *point sources*, so the observed

emission must be assumed to arise either homogeneously from the entire visible surface or from discrete regions that cover an unknown fraction of the stellar surface. In the first case, an atmospheric model based on the observed spectrum would describe only a crude mean structure of two regions with presumably very different physical characteristics. This crude mean would not be representative of either region. In the latter case, the area coverage (i.e. "filling factor") must be known *a priori* in order to derive a meaningful atmospheric model of the plage regions. A minimum prerequisite for any realistic model of stellar chromospheres is the determination of the filling factor of plages. However, even if this were known, the models would be realistic only if the emission came only from plages that have identical physical properties and are uniformly distributed over the star.

The generally accepted explanation of the optical variability of the most active late-type stars (e.g. RS CVn and BY Dra stars) is that their photospheres are non-uniformly covered with large, dark spotted areas. The rotational phase of light minimum indicates the hemisphere of maximum spottedness, and the total amplitude of the variation provides a lower limit to the area of spottedness. If the brightness of both spot and non-spot regions is known, the area of spots can be determined. Rodonò et al. (1986, Paper I) discussed the use of optical photometry in determining the spatial structure of stellar photospheres.

In an analogous way, the variation in ultraviolet emission line fluxes can provide a crude picture of the longitude of maximum chromospheric activity and the relative area of plage coverage. Again, the relative brightness of plage and non-plage chromosphere must be known before the absolute area of the plages can be inferred. Rodonò et al. (1987, Paper III) used the rotational modulation of ultraviolet emission line fluxes to study the chromospheric structure of II Pegasi, V 711 Tauri, and AR Lacertae. Byrne et al. (1987, Paper VI) used these results to derive mean chromospheric models for AR Lac and V 711 Tau and separate chromospheric models for the active and quiet hemispheres of II Peg.

A fundamental limitation of techniques that use the variability of total flux in some passband is that only a non-uniformly bright star will vary in total brightness as it rotates. The surface brightness distribution could be very inhomogeneous, but as long

---

[*] Based on observations collected with IUE at the ESA Satellite Tracking Station, Villafranca (Spain) and at NASA Goddard Space Flight Center, Greenbelt, MD, USA
[**] Guest Observer, the International Ultraviolet Explorer (IUE)

as the total visible spot or plage area on the visible hemisphere remains constant independent of rotational phase, there will be no variability. An absence of variation therefore does not imply an absence of spots or plages.

Vogt and Penrod (1983) and Vogt et al. (1987) described a method for determining not only the spotted area, but also the actual size and distribution of individual spots (or spot groups) across the stellar photosphere. Their technique, known as Doppler imaging, is to use the spectral line profiles of rapidly-rotating stars as one-dimensional velocity maps of their photospheres. By combining spectra obtained at many different rotational phases, they invert a series of observed spectra to derive a two-dimensional map of the brightness distribution.

We have developed a similar "spectral imaging" technique to determine the spatial distribution of the *chromospheres* of rapidly-rotating, late-type stars. Walter et al. (1987, Paper IV) used this technique to determine the chromospheric structure of AR Lac from a series of high-resolution spectra of the Mg II k line (2795.528 Å) obtained in October 1983, and Linsky et al. (1989, Paper X) used the technique to infer the location of a flare on V 711 Tau in October 1981.

In this paper we present spectral images of the chromosphere of AR Lac derived through an analysis of a series of 18 high-resolution ultraviolet spectra of AR Lac obtained in September 1985. Three discrete plage regions were isolated on the K 0 IV star of AR Lac. We determined the positions, sizes, and surface fluxes of these plages, as well as the surface flux of the mean K star chromosphere. We also determined that a large portion of the G 2 IV star is chromospherically inactive, and we present time-resolved spectra of an ultraviolet flare on the G star.

2. Observations and data reduction

2.1. The AR Lacertae binary system

AR Lacertae (HD 210334; HR 8448) is a bright ($V = 6.1$) eclipsing RS Canum Venaticorum system. We assume the system parameters summarized in Table 1 and given in Paper III and by Chambliss (1976). AR Lac is composed of two active, evolved stars – a G 2 subgiant and a K 0 subgiant. The system has a semimajor axis of 9.1 $R_\odot$, an inclination of 87°, and an orbital period of approximately 2 days. Both stars rotate synchronously with the orbital period. The time of primary eclipse ($\phi = 0.0$), based on photometry in 1981 and 1982 (Paper I), is determined by the ephemeris JD 2444977.0216 + 1.983170E. AR Lac is an atypical RS CVn-type system in that both stars are somewhat evolved and both exhibit strong stellar activity, but because of the eclipses it is an ideal system for an investigation of chromospheric structure (see Paper IV).

Table 1. AR Lacertae system parameters

Property	G 2 IV	K 0 III-IV
Mass ($M_\odot$)	1.35	1.36
Radius ($R_\odot$)	1.54	2.82
$v \sin i$ (km s^{-1})	40	72
K (km s^{-1})	116.1	115.6
V	6.94	6.75
B−V	0.68	0.93

Table 2. Log of September 1985 IUE observations

IMAGE	EXPOSURE START TIME (1985 UT) DAY	H M S	EXPOSURE TIME (min)	PHASE of mid exposure	Comments
LWP 6746	18 SEP	05 43 42	60	0.596	
SWP 26676a		06 55 35	30	0.62	
LWP 6747		07 34 01	60	0.635	
SWP 26676b		08 42 14	30	0.65	
LWP 6748		09 20 27	35	0.668	
LWP 6749		10 30 56	30	0.691	Not usable
LWP 6750		14 30 16	60	0.780	
SWP 26677a		15 37 39	30	0.80	
LWP 6751		16 16 27	60	0.818	
SWP 26677b		17 24 02	30	0.83	
LWP 6752		18 03 43	60	0.855	
SWP 26677c		19 11 07	30	0.87	
LWP 6753		20 05 27	60	0.898	
SWP 26678a		21 13 29	30	0.91	
LWP 6754		22 07 39	60	0.941	Partial Eclipse
SWP 26678b		23 23 45	30	0.96	Partial Eclipse
SWP 26678c	19 SEP	00 23 08	25	0.98	Total Eclipse
LWP 6755		00 57 28	54	0.999	Total Eclipse
SWP 26679a		02 03 30	27	1.02	Total Eclipse
LWP 6756		02 46 45	60	1.039	Partial Eclipse
SWP 26679b		03 54 56	30	1.06	Partial Eclipse
LWP 6757		04 34 31	60	1.076	Partial Eclipse
SWP 26679c		05 43 28	30	1.09	
LWP 6758		06 23 17	60	1.115	
SWP 26680a		07 36 37	30	1.13	
LWP 6759		08 13 10	60	1.153	
SWP 26680b		11 28 21	30	1.22	
LWP 6760		12 06 14	60	1.231	
SWP 26680c		13 16 13	30	1.25	
LWP 6761		14 40 24	60	1.278	
SWP 26681a		15 18 35	30	1.30	
LWP 6762		15 54 31	60	1.314	
SWP 26681b		17 01 57	30	1.33	
LWP 6763		17 47 35	60	1.354	
SWP 26681c		18 53 56	30	1.37	
LWP 6764		19 30 16	60	1.390	
SWP 26682a		20 36 31	30	1.41	
LWP 6765		21 32 30	17	1.425	Not Usable

2.2. The observations

AR Lac was observed continuously with the International Ultraviolet Explorer (IUE; see Boggess et al., 1978) for almost 40 hours during 18–19 September 1985. The observations began shortly after secondary eclipse and continued until just before first contact of the subsequent secondary eclipse (approximately 80% of an orbital cycle). We alternated between high-resolution LWP (1800–3200 Å; $\Delta\lambda \sim 0.2$ Å) and low-resolution SWP (1150–1900 Å; $\Delta\lambda \sim 6$ Å) spectra as summarized in Table 2 (to emphasize the time sequence of the observations, we refer to phases following primary eclipse as $1 + \phi$). We timed the exposures so that (1) two

short SWP spectra and one well-exposed LWP spectrum could be obtained during the total eclipse, and (2) new exposures were started at each contact of the eclipse.

2.3. Data reduction

The IUE images were reduced to calibrated spectra using standard software at the Colorado Regional Data Analysis Facility (RDAF), as described in Paper IV. Two of the 20 LWP spectra have very low S/N and are unusable, because the exposure times
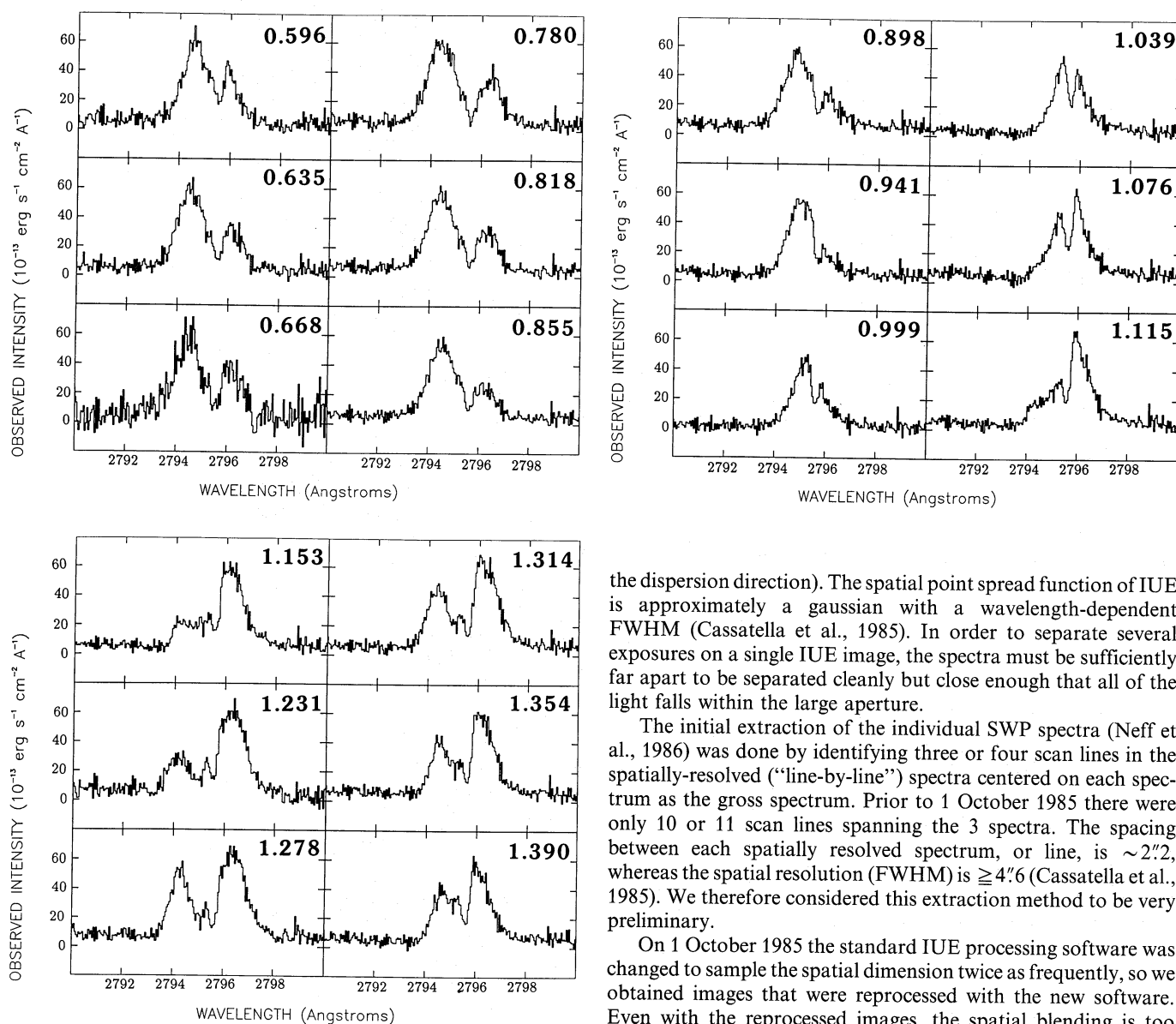
Fig. 1. The 18 Mg II k profiles of AR Lac obtained in Sep. 1985 are displayed here on a common scale. The orbital phase of mid-exposure is given in each panel

were limited by a high level of background radiation. The 18 reduced high-resolution spectra of the Mg II k emission line are shown in Fig. 1. Several interesting features can be seen in the reduced spectra: (1) A narrow interstellar absorption component is seen in all spectra. (2) The peaks in the overall line profiles shift in wavelength roughly in phase with the orbital motion of the two stars. (3) The total flux in the line is variable. (4) The post-eclipse spectra ($\phi = 1.039$ to 1.153) differ qualitatively from the (reflected) pre-eclipse spectra ($\phi = 0.855$ to 0.941) in that the G star flux seems decreased, and its profile is distinctly non-gaussian. (5) Excess emission is seen at the position of the G star between $\phi = 1.278$ and 1.390.

In order to increase observing efficiency, up to three individual spectra were obtained in each SWP image. Three individual spectra can be distinguished visually in these images, but the spectra are blended in the spatial dimension (i.e., perpendicular to

the dispersion direction). The spatial point spread function of IUE is approximately a gaussian with a wavelength-dependent FWHM (Cassatella et al., 1985). In order to separate several exposures on a single IUE image, the spectra must be sufficiently far apart to be separated cleanly but close enough that all of the light falls within the large aperture.

The initial extraction of the individual SWP spectra (Neff et al., 1986) was done by identifying three or four scan lines in the spatially-resolved ("line-by-line") spectra centered on each spectrum as the gross spectrum. Prior to 1 October 1985 there were only 10 or 11 scan lines spanning the 3 spectra. The spacing between each spatially resolved spectrum, or line, is $\sim 2\rlap{.}''2$, whereas the spatial resolution (FWHM) is $\geq 4\rlap{.}''6$ (Cassatella et al., 1985). We therefore considered this extraction method to be very preliminary.

On 1 October 1985 the standard IUE processing software was changed to sample the spatial dimension twice as frequently, so we obtained images that were reprocessed with the new software. Even with the reprocessed images, the spatial blending is too serious for the individual spectra to be extracted simply by co-adding lines from the line-by-line files (see Fig. 2). Instead, we fit three instrumental (gaussian) profiles in the spatial direction at each wavelength step to extract the intensities of the 3 spectra at that wavelength. This procedure was then repeated for every wavelength step to extract the 3 spectra.

We measured the FWHM of the approximately gaussian spatial profile from image SWP 26682 (a single spectrum), and we determined the spatial centers of the individual spectra from scans through the C IV (1550 Å) line, since the actual placement of the star at the standard offsets was only accurate to $\sim \pm 1$ line in the line-by-line files. We constrained the positions and widths of the three profiles to these values and then derived a least-squares fit for the intensities of the 3 gaussians. The integrated flux in each gaussian was then taken as the intensity at that wavelength for each spectrum. The same procedure was used to extract the two spectra in image SWP 26676 and the single spectrum in SWP 26682. The resultant spectrum for SWP 26682 was identical to that produced by the standard (IUESIPS) extraction, confirming the accuracy of our procedure. The background corrections and the flux calibrations were performed at the Colorado RDAF
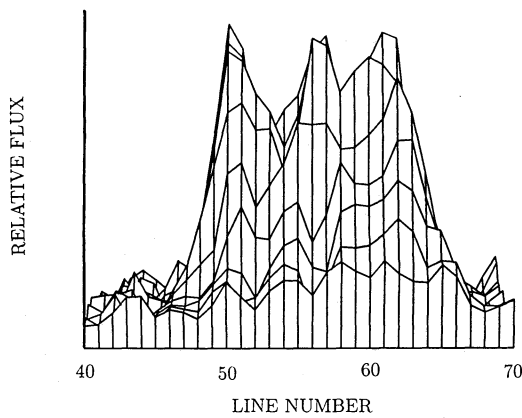
Fig. 2. Three spatially blended C IV emission lines are shown in this surface plot of a typical SWP image. Wavelength increases into the paper from 1540 Å, peaking at 1550 Å. The three spectra were obtained using the standard offset reference points

Fig. 3. The measured centroid velocities of the two gaussian emission components fitted in Round A compared to the known radial velocities of the K and G stars. Note the discrepancy between the measured and predicted K star velocities near $\phi = 0.75$

using the LOW procedure in the standard IUE software library. The measurement of integrated line fluxes was performed as described in Paper IV.

3. Data analysis

3.1. Spectral imaging of the Mg II k lines

The spectral imaging principle was discussed by Neff (1988). The procedure described in Paper IV was used to analyze the Mg II k lines. Several improvements have been made to the fitting code (Neff, 1987), but these did not alter the basic procedure in any way.

At first glance (Fig. 1), the 18 observed Mg II k line profiles can be characterized by two emission components at radial velocities corresponding roughly to the predicted orbital velocities of the two stars plus an unresolved interstellar absorption line. In the initial round of the analysis, three gaussian components were fitted to the observed profiles. The width of the interstellar absorption component was constrained to be the instrumental width.

In order for these three-component fits to provide an acceptable fit to the line profiles, (1) the measured velocities of the two emission components must agree (within observational uncertainty) with the predicted stellar velocities, (2) the widths of the components must be consistent with the stellar rotational velocities, and (3) the equivalent width of the interstellar absorption component must remain roughly constant. None of these conditions were met by the three-component fits.

Uniform emission across a stellar surface would produce a *symmetric* line profile centered at the stellar radial velocity. Large *non-uniformities* in brightness will produce emission components superimposed on the mean symmetric profile that vary in wavelength due to the Doppler shift produced by the star's rotation. The net profile will be asymmetric, and a single-component fit to this profile likely will not lie at the predicted stellar radial velocity. Therefore the non-uniform distribution can be mapped by fitting the observed profiles with a symmetric component centered at the stellar radial velocity plus additional components to account for the residual emission. In practice, the minimum number of additional components required to match
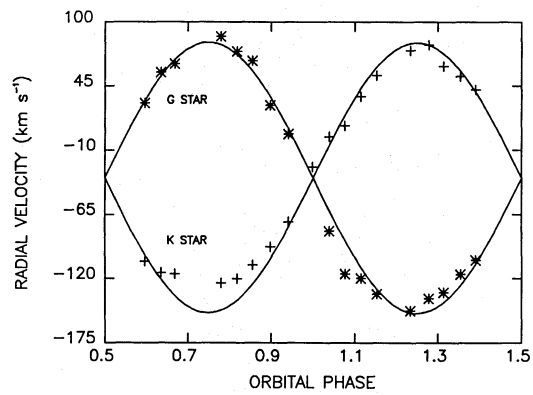
the observed profiles are determined iteratively, using an interactive multiple-component fitting routine. The primary constraints in this procedure are the central wavelengths of the uniform stellar components and the interstellar absorption equivalent width, which should remain constant. Secondary constraints are the rough constancy of the stellar emission line widths and smooth temporal variation of the stellar flux.

Each spectrum was fit in up to six subsequent "rounds". As many as 50 iterations (though typically 5 to 10) were required to obtain the best fit for each round, and the best fit in each round was taken as the initial estimate for the next round. To more fully illustrate our spectral imaging technique and to define our criteria for determining the best fits, we now discuss each fitting round in order.

3.1.1. Round A

The line profiles were initially fit with three gaussian components. Only the FWHM of the interstellar absorption line was constrained (to be the instrumental width-5 bins; about 0.25 Å). As noted for the October 1983 data (Paper IV), the overall shapes of the line profiles can be reasonably well matched by the sum of 3 gaussians – two emission components (which crudely follow the stellar positions) and an interstellar absorption component.

To investigate the quality of this round of fits, we first used the mean measured wavelength of the interstellar absorption line as a constant wavelength (and therefore velocity) reference. The difference between each interstellar wavelength measurement and the mean was then added to the measured wavelength of the two emission components to correct for any differences in the initial wavelength scales. These differences are small (typically about 1 bin) compared with the line widths and separations.

The measured centroid velocities of the two emission components roughly follow the known velocities of the two stars (Fig. 3). However, some measured velocities differed from the predicted velocities by amounts too large to be consistent with the simplest assumption that the observed profile is due to uniform emission from both stars. The most obvious discrepancy between the velocities of the measured emission components and the stellar orbital velocities is for the blueward (K star) component near $\phi = 0.75$, where the residual velocities are about 25 km s^{-1} (Fig. 3). If this emission component were constrained to be

centered at the predicted radial velocity of the K star, there would be emission on the red wing of this component far in excess of that on the blue wing; i.e., the profile would be highly asymmetric. The measured interstellar equivalent absorption widths at these phases are consistently smaller than the average. Since the interstellar absorption equivalent width must remain constant, a low absorption equivalent width indicates that this excess emission on the red wing of the K star profile must be even greater than the fits indicate.

The simplest way to match the velocities of the two emission components with the predicted stellar velocities near $\phi = 0.75$ and still have an acceptable fit to the observed line profiles is to add to the fit another emission component on the red wing of the K-star emission component.

3.1.2. Round B

In Round B, a fourth component was added to account for the asymmetric emission of the K star near $\phi = 0.75$. An additional component was also added to the G star between $\phi = 1.278$ and 1.390, to account for the flare emission. As in Round A, the only fixed parameter in these fits was the FWHM of the interstellar absorption component.

The fourth component reproduced the redward asymmetry of the K star component near $\phi = 0.75$, and the K star global emission component consequently followed its predicted radial velocity. Some small but systematic differences still remained between the measured and predicted radial velocities.

In order to evaluate the quality of these fits, we studied the resulting parameters of global emission features in more detail. Following eclipse, the global G star flux rose very slowly to near its pre-eclipse level until, at $\phi = 1.28$, there was a sudden increase and subsequent rapid decay due to a flare. The post-eclipse behavior of the G star line profile is very striking. At $\phi = 1.039$, 56% of the G star should be visible, yet no emission in excess of the K star wing is seen at the expected position of the G star. Hence, the visible portion of the G star at this phase *must be very dark* in the Mg II k line compared to the portion of the G star viewed before eclipse. Alternatively, material bound to the K star might be obscuring our view of the G star. The shape of the G star Mg II k flux vs. time curve can provide information about the spatial extent of this chromospherically very *inactive* region.

The K star flux was found to be systematically higher following eclipse. This could be due to a difference in brightness between the leading and trailing hemispheres, to additional emission from discrete regions that have not been fitted, or to temporal variability.

The deconvolved widths of the global K star components were systematically larger following eclipse. While it is unwise to presume specific values for the line widths, *variations* in the measured widths probably indicate the presence of additional emission components near the stellar limbs that have not yet been fitted. After applying the strong absolute constraints of stellar radial velocities and interstellar absorption line width (i.e., instrumental resolution) and equivalent width, the *relative* with and flux constraints can be used to develop and refine a self-consistent system model. The secondary nature of these constraints, however, cannot be overemphasized.

At total eclipse, when only the K star profile was seen, the emission profile was symmetric. If the redward asymmetry fitted at previous phases were due to excess emission from a discrete region on the K star, it must have rotated behind the limb by $\phi = 0.999$.

3.1.3. Round C

Only the pre-eclipse spectra were fitted in Round C. The mean radial velocity of the global K star component was constrained to lie within ± 10 km s^{-1} of its predicted value (the velocity was not strictly fixed, but fits not meeting this criterion were rejected). The Round C fits were evaluated primarily for a constant interstellar absorption equivalent width. Minor consideration was given to the global K star flux; it was permitted to vary, but radical changes between adjacent phases were not allowed.

The purpose of Round C was to determine the impact of adding a fifth component to better reproduce the asymmetry in the K star line profile at all phases. While the fifth component provided a more precise description of the phase-dependent asymmetry, it was equally clear that the global K star component must be more tightly constrained.

In a general way, the following features were identified in the first 3 fitting rounds: (1) at least two distinct, discrete emitting regions on the K star, (2) an inactive region on the G star or substantial absorption due to the K star circumstellar material, and (3) a flare on the G star. These identifications came about by assuming only that any *uniform* emission from the stars could be represented by a gaussian emission profile centered roughly at the predicted stellar radial velocities. It also appears that the global K star flux, and perhaps its width, was higher after eclipse than before.

The next phase of the analysis was to derive the properties of the discrete emission regions (i.e., plages) on the K star and to piece together a self-consistent model of the way in which the individual emission components make up the observed profile at all phases. This task requires that some of these constraints be formalized, i.e. that some of the parameters be fixed. Since the crude picture has already emerged, this should only serve to refine the picture.

3.1.4. Round D

The philosophy of Round D was to constrain the stellar radial velocities *exactly*, to use the interstellar equivalent width constraint, and to allow the additional "plage" components to vary in order to account for any asymmetry. Figure 4 shows the fluxes in the various components after the K star radial velocity was
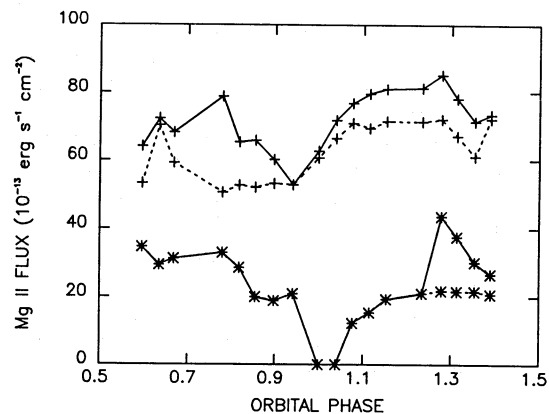

Fig. 4. The resulting fluxes from Round D are shown as dashed lines for the global components alone, and as solid lines for the total emission from each star. The plusses represent the K star, and the asterisks represent the G star. The K star fluxes at $\phi = 0.635$ and 1.390 seem to be inconsistent with those at neighboring phases

constrained at its predicted orbital value and the fits were required to have a roughly constant interstellar absorption equivalent width. An additional gaussian component was added to the post-eclipse spectra to account for the variation in flux and width of the K star profile. If the plage flux was underestimated at $\phi = 0.635$ and 1.390, then the global K star flux was constant from the start of the observations until $\phi = 0.999$ (see Fig. 4). It subsequently rose linearly to a high level between $\phi \sim 1.1$ and 1.3 and then decayed back to its low level. The G star flux at $\phi = 0.941$ is likely overestimated, because the global stellar profiles are blended at this partial eclipse phase, and we fit a *symmetric* component to the G star emission, even though 25% of the G star was occulted by the K star at this phase. Since this fit slightly underestimates the observed profile, we conclude that the K star plage flux (the plage component lies at the same wavelength as the occulted portion of the G star) is slightly greater than 25% of the integrated G star flux, and the G star flux is 25% lower than shown. In the next fit round, we attempted to increase the plage flux at phases 0.635 and 1.390, and we assigned the excess flux at $\phi = 0.941$ to the plage.

We determined the position, width, and flux of the flare component by subtracting the pre-flare G star profile ($\phi = 1.234$) from the spectra between $\phi = 1.278$ and 1.390. The flare emission component decayed in width as well as in flux.

Three discrete plage components on the K star were fitted in Round D. The existence of the third plage was required primarily by the constraint of constant interstellar equivalent width during the post-eclipse phases. The large plage seen on the red wing prior to eclipse was seen to reappear 0.5 phase later on the blue wing in the last few spectra (again near the interstellar position).

3.1.5. Rounds E and F

The primary purpose of Round E was to see if by increasing the plage flux at $\phi = 0.635$ and 1.390, we could still obtain an adequate fit to the profiles and still maintain a self-consistent fit to the global parameters. Three discrete plage features on the K star, a flare on the G star, and either an inactive patch on the G star or K star circumstellar absorption already have been identified. The uniform, global emission of both stars also has been characterized. All of this has been done in a manner that is in principle reproducible and probably unique (in that all of the features are required to match the basic assumptions).

The final fitting round (Round F) was intended to resolve any remaining variations in the measured parameters from one spectrum to the next, to determine how much the previously constrained parameters can be relaxed, and to arrive at a final series of fits that include all of the components of the system while obtaining the best possible fits to the profiles. As such, the measured parameters in the last round would probably be slightly different if this fit round were independently repeated. Nevertheless, the basic system model, developed in Rounds A through E, should not change. The "artistic" freedom applied in the last round (albeit minor) characterizes the degree of uncertainty in the measured parameters.

The final series of fits are shown in Fig. 5. The global G star emission has been subtracted from the last four spectra in Fig. 5 in order to illustrate the flare component.

3.2. Rotational modulation of the SWP line fluxes

Figure 6 shows the integrated line fluxes for C IV (1550 Å) and C II (1335 Å). The total eclipse of the G star and the flare dominate the observed flux variability. However, the emission level between $\phi = 0.80$ and 0.91, when the total plage flux was highest, is substantially higher than at those phases where no discrete plages were visible.

Guided by the analysis of the Mg II k spectra, we assumed that the total eclipse phases include only global K star emission (i.e., that no plages are visible on the K star), that only the global K star and G star spectra are seen at $\phi = 0.62$ and 1.41, and that the additional emission from $\phi = 0.80$ to 0.87 (SWP 26677) is due only to the plages. The far-ultraviolet spectra of the mean K star, the mean G star, and the plage regions were then determined as described in Paper IV. A flare-peak spectrum was derived by subtracting the pre-flare spectrum from the flare-peak spectrum.

4. Results

Tables 3 and 4 summarize the parameters derived from the final series of fits to the Mg II k lines (see Fig. 5). The integrated emission line fluxes for the strongest lines in the far-ultraviolet spectrum are listed in Table 5. Using the final parameters of the multiple gaussian-component fits to the Mg II k lines, together with the rotational modulation of the SWP line fluxes, we were able to map the spatial brightness distribution of the chromospheres of the two stars in the AR Lac system at this epoch, to determine the ultraviolet line surface flux for each atmospheric component as a function of time or phase, and to study the rise and decay of the G star flare.

4.1. Component fluxes

Figure 7 shows the integrated Mg II k flux as a function of time (orbital phase) for each component. The top curve, the total flux emitted by the system, is a photometric result (corrected for interstellar absorption). Without redundant phase coverage, it is not possible to distinguish with certainty between temporal variations and variations caused by the rotation of stars with non-uniform but time-invariant atmospheres. Nevertheless, primary eclipse is clearly visible, and there is a flare-like peak at $\phi \cong 1.278$. There is also significant variability that is neither eclipse- nor flare-related.

The essence of spectral imaging is to study this flux variation as a function of *wavelength*, not just of time or orbital phase, in order to map the spatial structure of the atmosphere. The individual curves in Fig. 7 represent the flux variation in the global stellar and in the discrete plage components. Our interpretation that the modulation of the total flux is due to the rotation of discrete regions does not require redundant phase coverage, because the emission clearly is not symmetric about the stellar positions. The interpretation of these discrete regions as *long-lived* plages would be greatly strengthened, however, if the same behavior were seen to repeat during successive orbits.

The global K star emission flux has a high state ($70.6 \pm 1.5 \ 10^{-13} \ \mathrm{erg \, s^{-1} \, cm^{-2}}$; all reported errors are $\pm 1\sigma$ scatter about the mean values and do not include a contribution due to possible systematic errors in the absolute flux scale) between $\phi \cong 1.10$ and 1.28. The low state ($50.5 \pm 1.5 \ 10^{-13} \ \mathrm{erg \, s^{-1} \, cm^{-2}}$) ranges from at least $\phi = 0.596$ to 0.941, and perhaps from $\phi \sim 0.4$ to $\phi \sim 1.0$. We treat this as a difference between the leading (low state) and the trailing (high state) hemispheres. The surface flux difference is 40% if the high-state emission is from the entire hemisphere, or larger if the excess emission is from a more compact region. The phases of the rise and fall of the flux indicate that the high state is not from the entire hemisphere, but rather
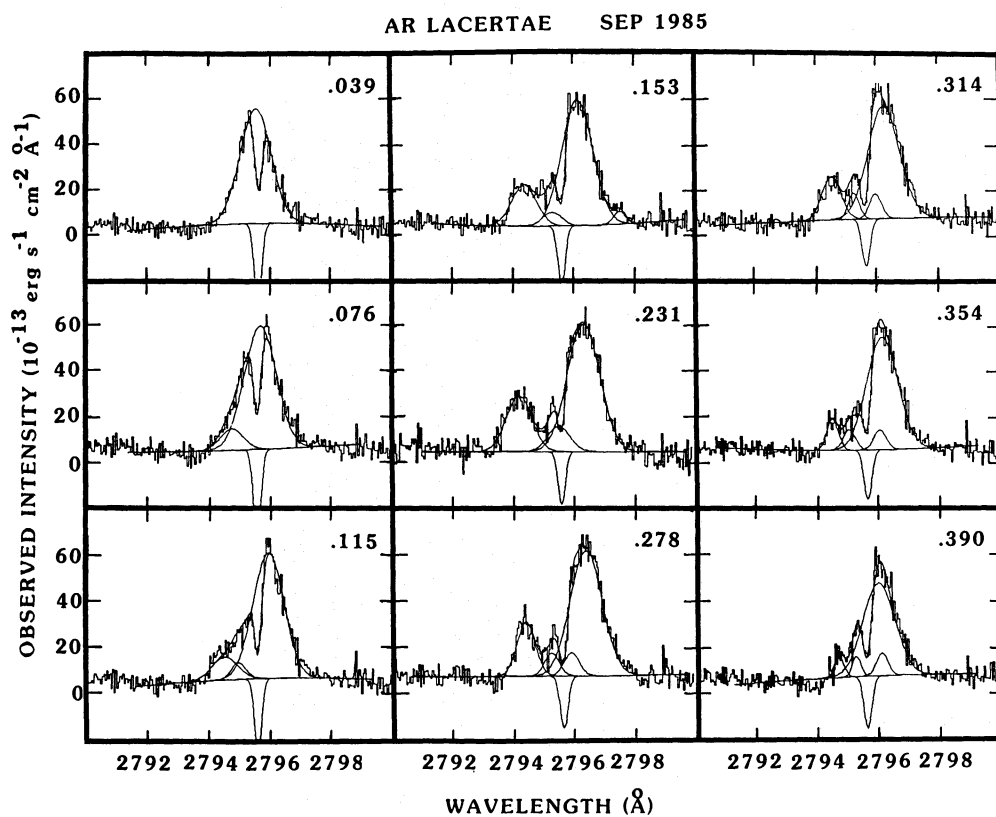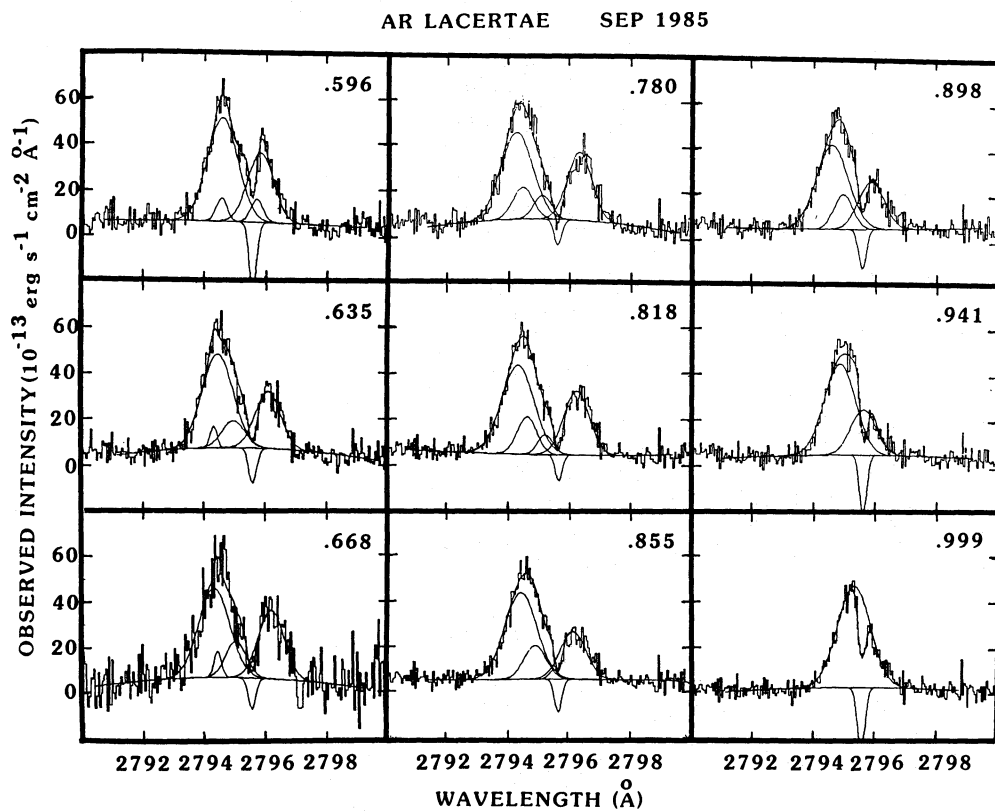
AR LACERTAE   SEP 1985

AR LACERTAE   SEP 1985

Fig. 5. The final fits to the 18 observed spectra. At $\phi = 0.941$ the G star is shown as a symmetric profile even though the star is partially eclipsed. The pre-flare G star profile was subtracted from the spectra between $\phi = 1.278$ and 1.390 prior to the fittings
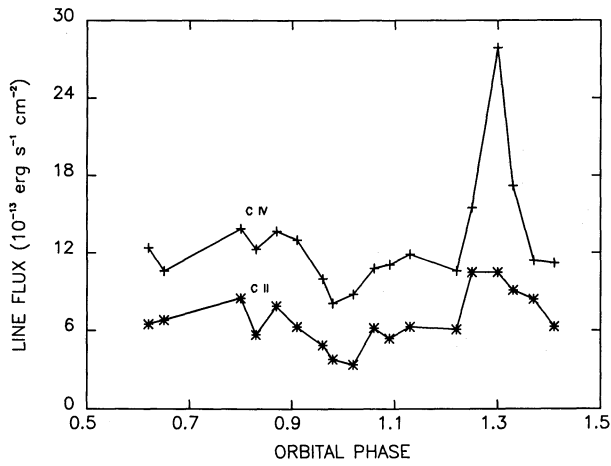
Fig. 6. The modulation of C IV (top) and C II fluxes was dominated by the flare and the eclipse, but the flux was enhanced at phases where the plages, as seen at Mg II, were brightest. The flare must have occurred very near the end of SWP 26680c ($\phi = 1.25$). The relative flare enhancement for C IV is higher than for C II. The flare decay is faster for C IV than for C II

from a region extended $\sim 55°$ in longitude and centered at phase ~ 1.2 (longitude 70°). A region this extended would not be expected to produce discrete features in the profile at the spectral resolution and S/N of IUE, but rather (as was seen) a global brightening. A lower limit to the mean surface flux can be derived by assuming that the global emission arises *homogeneously* from the entire hemisphere. The minimum surface fluxes are $23 \ 10^5 \, \mathrm{erg \, s^{-1} \, cm^{-2}}$ for the low state and $32 \ 10^5 \, \mathrm{erg \, s^{-1} \, cm^{-2}}$ for the high state. Of course the emission could arise from an inhomogeneous atmosphere with regions of higher surface flux.

While the G star global flux prior to eclipse was roughly constant ($29.3 \pm 2.1 \ 10^{-13} \, \mathrm{erg \, s^{-1} \, cm^{-2}}$), immediately following 4th contact its flux was about half that value. In addition, the three Mg II k spectra obtained immediately after 4th contact show little emission from the blue side of the G star line profile. At $\phi = 1.039$, when 56% of the G star should have been visible, *no Mg II k emission attributable to the G star was seen at all.* The simplest explanation of this behavior is a dark (chromospherically inactive) patch on the G star. An absolutely black, circular patch extending from longitudes 335° to 75° could produce all of the observed variation in the light curve and line profiles. In the absence of the

Table 3. Spectral imaging results: global components

PHASE	λ_K	λ_G	W_K	W_G	F_K	F_G	EW
0.596	4.530	5.803	75	60	50.8	31.6	−0.22
0.635	4.415	6.062	74	59	51.4	25.0	−0.19
0.668	4.284	6.154	75	60	49.6	31.2	−0.17
0.780	4.203	6.271	77	58	50.1	29.9	−0.18
0.818	4.249	6.177	79	60	51.9	28.8	−0.16
0.855	4.367	6.083	78	62	50.8	22.2	−0.17
0.898	4.553	5.838	78	60	49.0	22.1	−0.15
0.941	4.810	5.582	74	−a	50.1	20.1	−0.18
0.999	5.302	−b	79	−b	59.8	−b	−0.19
1.039	5.487	−c	76	−c	65.6	−c	−0.20
1.076	5.652	4.718	78	54	71.1	8.9	−0.21
1.115	5.910	4.482	74	62	69.0	10.7	−0.19
1.153	6.089	4.326	75	59	70.0	18.8	−0.20
1.234	6.270	4.144	77	60	73.1	25.4	−0.20
1.278	6.340	4.121	76	61	69.8	23.7	−0.22
1.314	6.188	4.191	76	61	63.4	23.9	−0.18
1.354	6.095	4.401	74	58	62.3	23.4	−0.19
1.390	5.955	4.553	76	60	52.0	25.2	−0.19

^{a} G star partially eclipsed
^{b} G star totally eclipsed
^{c} G star partially eclipsed but not seen
UNITS:
λ (Mg II k wavelength−2790 Angstroms): Å
W (deconvolved $v \sin i$): km s^{-1}
F (integrated Mg II k line flux): 10^{-13} erg s^{-1} cm^{-2}
EW (equivalent width of interstellar absorption line): Å

Table 4. Spectral imaging results: plages

Phase	λ_A	W_A	F_A	λ_B	W_B	F_B	λ_C	W_C	F_C
0.596	4.588	18	6.0	3.994	U	1.4	5.688	25	5.2
0.635	4.939	54	10.8	4.286	U	2.6	−	−	−
0.668	4.998	48	13.3	4.401	U	3.5	−	−	−
0.780	5.057	47	11.7	4.414	39	7.5	−	−	−
0.818	5.160	33	5.4	4.559	45	13.1	−	−	−
0.855	5.465	13	1.7	4.841	52	13.7	−	−	−
0.898	−	−	−	4.921	43	12.0	−	−	−
0.941	−	−	−	−a	−a	≥ 7	−	−	−
0.999	−	−	−	−	−	−	−	−	−
1.039	−	−	−	−	−	−	−	−	−
1.076	−	−	−	−	−	−	−	−	−
1.115	−	−	−	−	−	−	4.927	32	4.5
1.153	−	−	−	−	−	−	5.242	44	4.9
1.234	−	−	−	−	−	−	5.451	52	10.0
1.278	5.207	32	6.1	−	−	−	5.862	33	6.3
1.314	5.184	20	5.2	−	−	−	5.896	23	5.4
1.354	4.998	24	4.5	−	−	−	6.002	24	4.3
1.390	5.209	9	3.1	−	−	−	6.050	22	4.7

U = Unresolved
^{a} Partial eclipse; plage not fitted; flux inferred
UNITS:
λ (Mg II k wavelength−2790 Angstroms): Å
W (deconvolved $v \sin i$): km s^{-1}
F (integrated Mg II k line flux): 10^{-13} erg s^{-1} cm^{-2}

Table 5. Measured SWP line fluxes $10^{-13}\,\mathrm{erg\,s^{-1}\,cm^{-2}}$

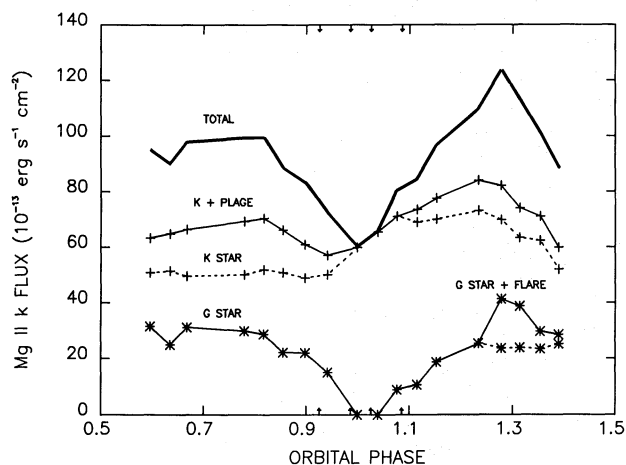| PHASE	N V 1240	O I 1305	C II 1335	Si IV 1396 +1402	C IV 1550	Si II 1808 +1817
0.62	1.7	2.0	6.5	–	12.4	5.4
0.65	–	3.8	6.8	3.8	10.6	4.6
0.80	3.3	4.9	8.5	2.0	13.9	6.7
0.83	1.6	2.9	5.7	3.7	12.3	6.2
0.87	1.5	3.6	7.9	4.8	13.7	5.4
0.91	1.2	4.5	6.3	3.5	13.0	5.4
0.96	–	4.0	4.9	2.3	10.0	4.2
0.98	–	2.9	3.8	1.5	8.1	4.4
1.02	1.8	2.3	3.4	1.9	8.8	3.8
1.06	–	3.7	6.2	2.2	10.8	5.1
1.09	1.2	3.3	5.4	–	11.1	5.3
1.13	–	3.6	6.3	1.4	11.9	5.4
1.22	–	4.2	6.1	2.8	10.6	4.1
1.25	2.2	4.7	10.5	3.3	15.5	6.0
1.30	4.0	4.6	10.5	5.3	27.9	7.0
1.33	2.6	3.9	9.1	6.0	17.2	7.6
1.37	1.7	4.7	8.4	3.5	11.4	6.0
1.41	1.0	3.0	6.3	2.0	11.2	5.4

Fig. 8. The velocities of the G star (solid line) and the plages are shown in the K star rest frame. The plages fall along 3 distinct rotational curves. In this and subsequent figures, plage A is represented by plusses and a short-dashed line, plage B by asterisks and a medium-dashed line, and plage C by X's and a long-dashed line. The plage velocity curves are only plotted where the plage is on the visible hemisphere. The equatorial rotational velocity of the K star is $\sim 72\,\mathrm{km\,s^{-1}}$. Horizontal lines are drawn at $\pm 72\,\mathrm{km\,s^{-1}}$ to illustrate that the amplitude of the radial velocity variations for plages A and C exceed that predicted by solid-body rotation of plages located on the equator and on the photosphere

eclipse, such a patch would modulate the total flux from the "normal" level ($\sim 30\ 10^{-13}\,\mathrm{erg\,s^{-1}\,cm^{-2}}$) to a minimum of $\sim 7\ 10^{-13}\,\mathrm{erg\,s^{-1}\,cm^{-2}}$. The global surface flux of the "normal" G star ($44\ 10^5\,\mathrm{erg\,s^{-1}\,cm^{-2}}$ assuming homogeneous emission) is 90% higher than the low state of the K star and 40% higher than the high state.

4.2. Plage positions

The relative velocities of the three discrete emission components (excluding the flare components), are shown in the velocity frame of the K star in Fig. 8. The thin solid line is the relative velocity of the G star. The components have been grouped into three distinct groups, represented by different symbols, because their velocities can be well represented by the rotational velocities of 3 distinct locations on the K star (dashed lines). We shall refer to the individual components as plages A, B, and C.

The longitudes of the plages are determined by the phase of the best fit solid-body (sinusoidal) rotation curves. The amplitude of the solid-body rotation curves are the product of the height above the photosphere, the stellar $v \sin i$, and the cosine of the latitude. The stellar $v \sin i$ is well known, but there is no way to distinguish *a priori* between height and latitude. However, amplitudes less than $v \sin i$ (e.g. plage B) indicate that the plage lies at high latitude. The minimum latitude can be determined by assuming that the plage lies on the photosphere. Radial velocity amplitudes greater than the stellar $v \sin i$ (e.g. plages A and C) imply that the plage must lie well above the photosphere, with the minimum height determined by assuming that the plage is equatorial. There is no way to distinguish between north and south latitudes, because the inclination of AR Lac is nearly 90°.

Plage longitudes are determined to $\sim \pm 10°$. It is not possible to estimate the uncertainty in the latitude or height determinations individually, but the amplitude of the radial velocity curves are

Fig. 7. The integrated Mg II k flux in each component is plotted as a function of time, with $\phi > 1$ following total eclipse to indicate the time sequence of the observations. The top curve is the total Mg II k emission from the system (observed flux corrected for interstellar absorption). The plusses indicate emission from the K star, and the asterisks indicate emission from the G star. The solid lines show the total emission from each star (including plages and flare), while the dashed lines show only the emission from the global (uniform) components. The phases of 1st through 4th contacts are indicated by arrows
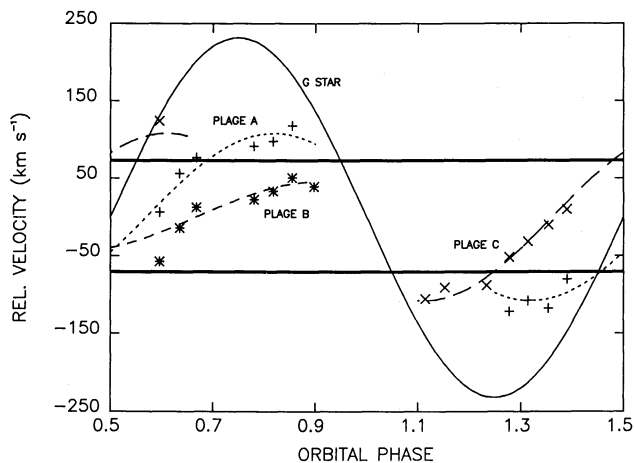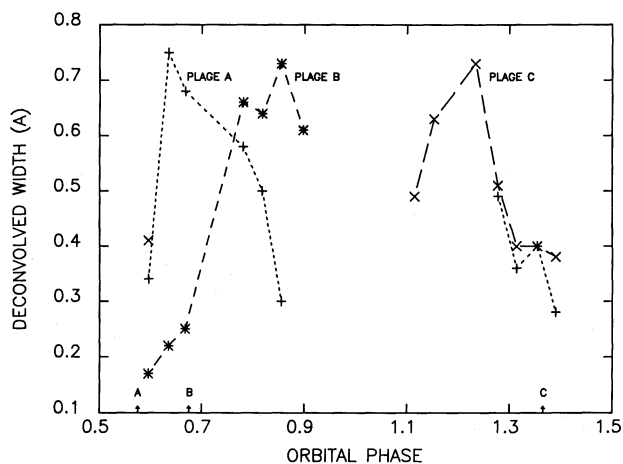
Fig. 9. The deconvolved widths (in Å) of the plage emission components vary, but their minimum values should provide a good measure of their longitudinal extents. When the plages were widest, they were also brightest, suggesting an additional broadening mechanism. The line and symbol types are consistent with Fig. 8. The arrows indicate the phase of central meridian transit for each plage

Fig. 10. The plage fluxes vary considerably on a short timescale. It is unlikely that this variation is spatial (i.e., center-to-limb behavior), but only observations over several orbits will allow any center-to-limb variability to be unambiguously distinguished from temporal variability. The line and symbol types are consistent with Fig. 8, and the phase of central meridian transit for each plage is marked with an arrow

determined to $\sim \pm 10\,\mathrm{km\,s^{-1}}$. Fitting the observed radial velocities to solid-body rotation curves is the simplest method for determining the plage positions. Differential rotation, ordered flows, limb brightening, and velocity smearing due to finite plage size could contribute systematic errors to this procedure. We believe that the systematic errors are substantially higher than the RMS measurement uncertainties. Better phase coverage and observations of systems that are inclined by various degrees to the line of sight would allow some of these important properties to be measured independently.

4.3. Plage widths and sizes

The radial velocity curves shown in Fig. 8 provide the *locations* of the surface features, but we desire to produce a crude image of the stellar surfaces. To do this, we must first measure the plage *sizes*. The total time required for a plage to transit the disk depends somewhat on its longitudinal extent, but this is subject to the same systematic uncertainties as the position determination.

We used the line widths of the plage emission components, after deconvolution of the instrumental profile (Fig. 9), to determine their extension in longitude. We assume that all of the deconvolved component width is due to velocity smearing from a resolved region on the star. These measured sizes are upper limits, because there could be a substantial intrinsic width (i.e., turbulence and flows) and the regions might not be homogeneous. These widths vary with orbital phase, but the minimum width should provide the best limit to the amount of rotational smearing and therefore the plage sizes.

There is no way to determine the latitudinal extent of the plages, since the inclination of AR Lac is $\sim 90°$. Therefore, we assume that the plages are circular.

Assuming circular plages and given the longitudinal extents, we can derive the plage areas. In this way, we determined the filling factors (fraction of visible hemisphere occupied by plage) to be 0.06 for plage A, 0.02 for plage B, and 0.09 for plage C. These filling factors are probably upper limits to the true filling factors, because we have assumed zero intrinsic width of the emission and
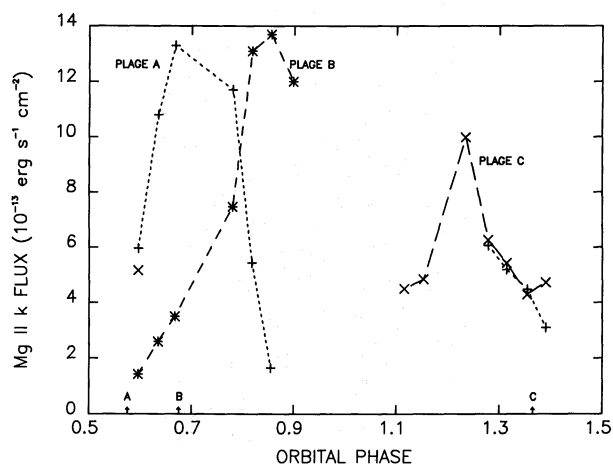
Table 6. Plage parameters

Plage	Longitude	Latitude	Filling Factor	Height R/R$_\star$
A	205	0	.06	1.5
B	240	±50	.02	1.0
C	130	0	.09	1.5

homogeneous plages. We use these filling factors to convert from the observed flux to the minimum surface flux.

4.4. Plage fluxes

The fluxes of the individual plages as a function of phase are shown in Fig. 10. At first glance, it appears that plages A and B are severely limb brightened. Certainly the plage contribution to the total flux near $\phi = 0.8$, when they are near the limb, is the highest for any phase. A more conservative interpretation is that the variability is temporal. In support of this interpretation, plage B was not as bright prior to central meridian passage as after, and plage A was not as bright after it reappeared on the blue limb as it was before it disappeared behind the red limb. A slight extension of the phase coverage would have resolved any ambiguity between temporal and center-to-limb behavior. The inferred positions and sizes of the plage components are listed in Table 6.

4.5. G star flare

The parameters of the flare component (Fig. 11 and Table 7) were determined by subtracting the pre-flare G star profile from the last 4 spectra and then fitting the residual emission. Since the G star flux at $\phi = 1.231$ had not yet returned to its "normal" level, it is possible that this procedure slightly overestimates the flux in the flare component, but not by more than the measured flare flux at $\phi = 1.390$. Nevertheless, its flux and width can be determined rather accurately.
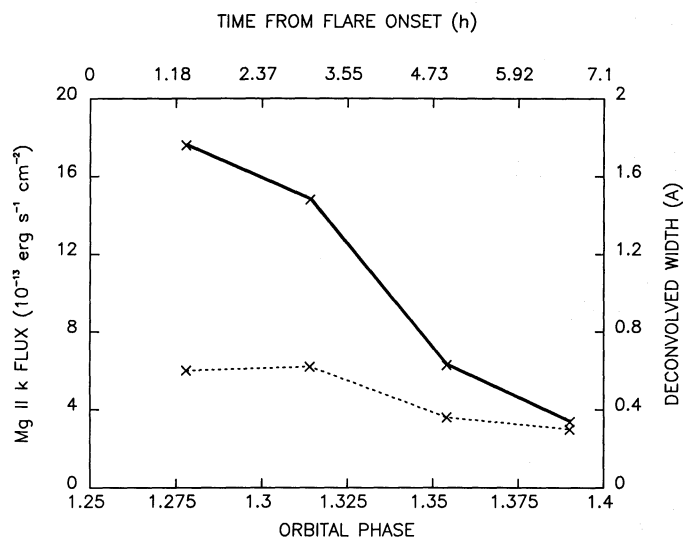
TIME FROM FLARE ONSET (h)

Fig. 11. The flux (solid line) and width (dashed line) of the flaring component alone were determined by subtracting the pre-flare G star profile from the observed profile and then fitting the residual emission with a gaussian. The probable phase of flare onset was $\phi = 1.255$, as indicated by the rise in flux in spectrum SWP 26680C
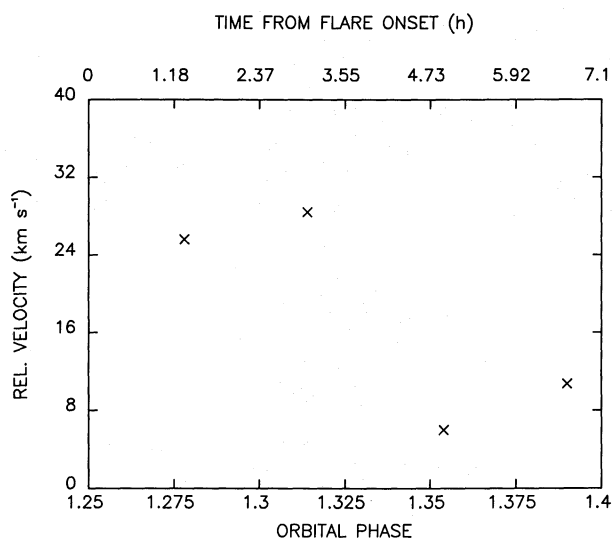
TIME FROM FLARE ONSET (h)

Fig. 12. The radial velocities of the flare component relative to the centroid velocity of the G star

Table 7. Flare parameters

PHASE	Mg II k FLUX[a]	DECONVOLVED WIDTH[b]	FILLING FACTOR
1.278	17.6	62	broadened
1.314	14.8	67	broadened
1.354	6.3	31	0.03
1.425	3.4	20	0.01

[a] 10^{-13} erg s^{-1} cm^{-2}
[b] km s^{-1}

We can estimate the maximum area (filling factor = 0.01 to 0.03) of the flaring region from the Mg II k line width in the latest decay phases by assuming that the width is due only to rotational smearing and that the region is circular. The line width of the flare component near peak flux is 62 km s^{-1}, indicating the presence of an additional broadening mechanism.

If the filling factor is 0.01, the Mg II k surface flux in the flare at $\phi = 1.278$ was $2.7 \, 10^8$ erg s^{-1} cm^{-2}, nearly 100 times higher than the mean non-flaring level from the G star. The observed $1/e$ decay timescale of the flare at Mg II k is ~ 3.5 h. The rise time to peak flux is < 2.4 h ($\Delta\phi = 0.044$), and the decay time to the pre-flare flux level is between 5.3 ($\Delta\phi = 0.11$) and 9.1 ($\Delta\phi = 0.19$) h. The minimum total radiative energy output in the Mg II k line during the flare was $2.5 \, 10^{31}$ erg.

At flare peak, the measured radial velocity of the flare component (Fig. 12) was redshifted about 25 km s^{-1} with respect to the central meridian of the G star. At the end of the flare, the measured relative velocity was $\sim +10$ km s^{-1}. This difference cannot be explained simply by the rotation of a discrete region, which should change in velocity by about the same amount but in the opposite sense in this phase interval. This difference is direct evidence that there was a systematic redshift of the flare emission

of $\geqq +30$ km s^{-1} near the flare peak. Similar systematic redshifts have been seen in flares on other systems (e.g. Simon et al., 1980; Paper X; Neff et al., 1988). We have too few observations to determine accurately the position of the flaring region, but its longitude is best constrained by the measured radial velocities of the last two flare spectra, when the systematic flow velocity was a minimum, by assuming that the flare occurred near the equator and not far above the photosphere.

4.6. Interstellar medium

The mean wavelength of the interstellar absorption feature is 2795.570 ± 0.025 Å ($\pm 1\sigma$), which corresponds to a heliocentric flow velocity of $+4.5 \pm 2.7$ km s^{-1}. The mean measured equivalent width is -0.19 ± 0.02 Å. Böhm-Vitense (1981) and Crutcher (1982) predict a mean interstellar medium velocity of $+5$ km s^{-1} and -8 km s^{-1}, respectively, in this line of sight.

4.7. Spectral images

We have assimilated all of the information given in Sect. 4 into a series of Mg II k "images" of the AR Lac system (Fig. 13; see also Neff and Neff, 1987). The relative sizes and positions of the two stars, the plages, and the flare are accurately depicted. The relative surface fluxes in each region are represented with a linear gray scale. Plage C is seen on the limb of the K star at $\phi = 0.596$. It reappears at $\phi = 1.115$. Plage A is seen between $\phi = 0.596$ and 0.858, and plage B is seen between $\phi = 0.596$ and 0.898. The flare is seen on the G star from $\phi = 1.278$ to 1.390.

4.8. Transition region line fluxes

The integrated line fluxes of the far-ultraviolet lines are presented in Table 5. As described in Sect. 3.2, we determined the spectra of the plage, flare, and global stellar components individually. The far-ultraviolet surface fluxes from each component, listed in Table 8, were computed using the filling factors determined for
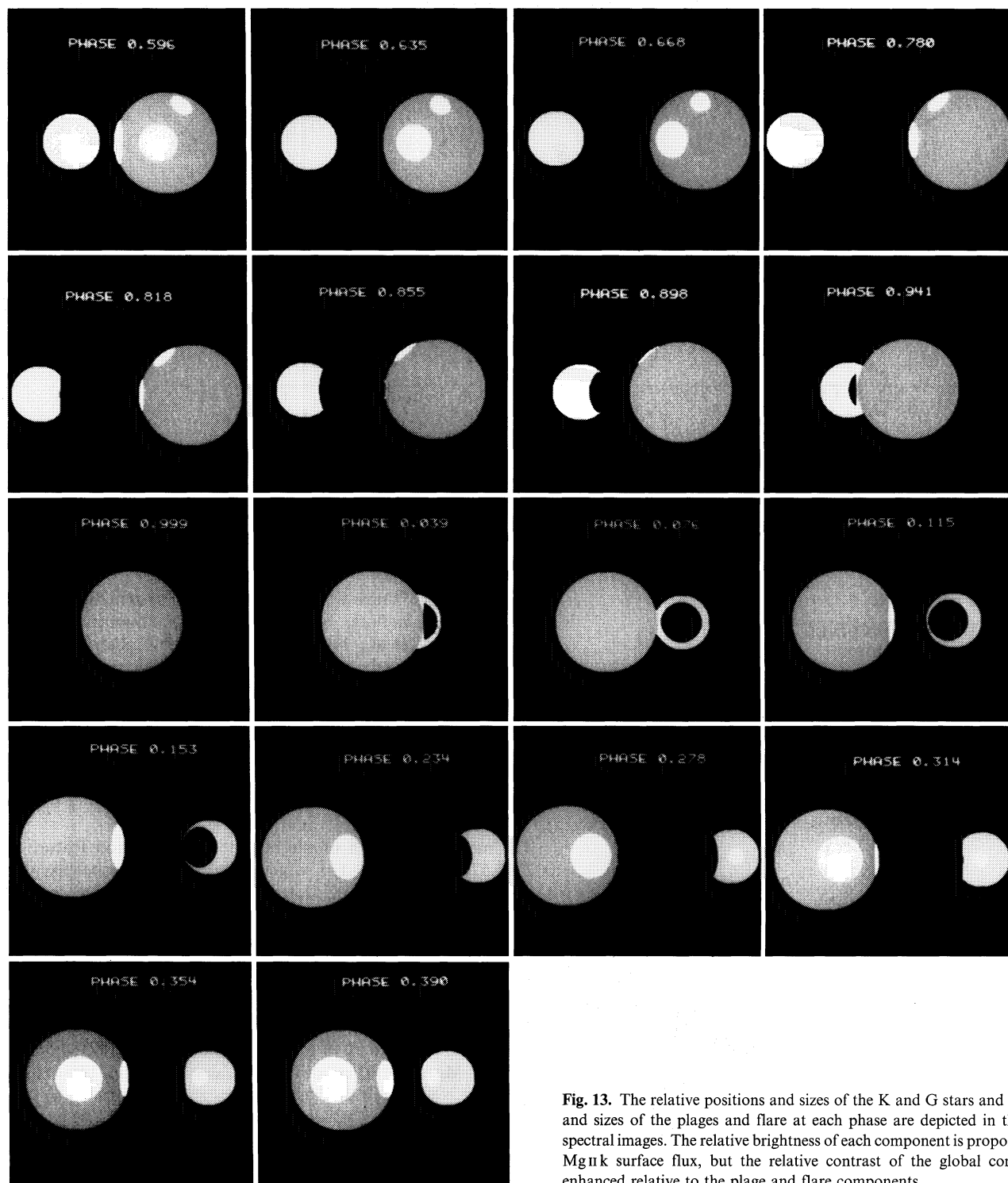
Fig. 13. The relative positions and sizes of the K and G stars and the location and sizes of the plages and flare at each phase are depicted in this series of spectral images. The relative brightness of each component is proportional to its Mg II k surface flux, but the relative contrast of the global components is enhanced relative to the plage and flare components

Mg II k. The Si III] and C III] fluxes were measured only in the co-added spectra obtained at total eclipse (K star only), the flare peak, the K plus G plus plage (SWP 26677), and the global K plus G (SWP 26682). C III] was not detected in any of these spectra, so only upper limits are quoted. These lines are included in Table 8 because their ratio provides an important density diagnostic. With

low-resolution SWP spectra, we are not able to derive any information on line positions or widths.

The SWP spectra provide further constraints on the rise and decay of the flare. The flare must have occurred very near the end of SWP 26680c ($\phi = 1.25$), because there was an observable enhancement of the SWP lines at this phase. LWP 6760 ($\phi = 1.278$)

Table 8. Component surface fluxes

Line	f_K	f_G	F_K	F_G	f_P^a	F_P	$\frac{F_P}{F_K}$
N V	1.8	< 1	0.8	< 1.5	1.1	6.3	7.6
C IV	8.4	2.5	3.8	3.8	2.4	13.7	3.6
Si IV	1.7	1.2	0.8	1.8	0.6	3.4	4.4
C III	<0.1–0.3	<0.1					
Si III	0.5–0.9	0.3–0.7					
C II	3.6	3.0	1.6	4.5	0.8	4.6	2.8
Si II	4.1	0.9	1.9	1.4	1.1	6.3	3.4
Mg II	50.5–70.6	29.3	23.0–32.2	44.2	19.2	109	3.4–4.7

Observed line fluxes (**f**) are in units of 10^{-13} erg s^{-1} cm^{-2}
Surface fluxes (**F**) are in units of 10^5 erg s^{-1} cm^{-2}

[a] Plage A + Plage B

therefore was started shortly after the peak of the flare, which must have occurred at $\phi \sim 1.255$. The hotter lines (N v, C iv, and Si iv) are enhanced by greater factors and seem to decay more rapidly than the cooler lines (C ii, Si ii), as seen by Walter et al. (1984) for the September 1984 flare on AR Lac and for the October 1981 flare on V 711 Tau (Paper X).

5. Conclusions

We have determined the spatial distribution of the chromospheric emission from the AR Lac binary system in September 1985. The trailing hemisphere of the K 0 IV star was globally 40% brighter than the leading hemisphere. The G 2 IV star also showed a large variation in global brightness (a factor of 3), attributable to a large, chromospherically inactive region on its surface. There were 3 distinct regions on the K star surface that were measurably brighter than the surface mean. We measured the location, size, and surface flux of each of these regions. We also were able to constrain the size, location, and surface flux of a region on the G star that flared during our observations. The peak surface flux in the flare was ≥ 100 times greater than the mean surface flux from the G star. Substantial line broadening and a systematic redshift of the flare emission was observed near the time of peak intensity.

These results are based on a series of 18 high-resolution spectra obtained at a single epoch. The observations covered 80% of a single orbital cycle. The images thus describe the system only as it appeared during the 40 h period that we observed. We cannot conclude with these observations alone that this structure is due to stable active regions that last over many orbital cycles. Indeed, the flux from the plage regions varies considerably on an orbital timescale. Nevertheless, two of the regions were seen to reappear approximately half an orbital period after they disappeared from the visible surface. The similarity of our results with those in Paper IV suggest that the individual plage components are indeed long-lived, but further observations at a later epoch are required to confirm this suggestion.

References

Boggess, A. et al.: 1978, *Nature* **275**, 372
Böhm-Vitense, E.: 1981, *Astrophys. J.* **244**, 504
Byrne, P.B., Doyle, J.G., Brown, A., Linsky, J.L., Rodonò, M.: 1987, *Astron. Astrophys.* **180**, 172 (Paper VI)
Cassatella, A., Barbero, J., Benvenuti, P.: 1985, *Astron. Astrophys.* **144**, 335
Chambliss, C.R.: 1976, *Publ. Astron. Soc. Pacific* **88**, 762
Crutcher, R.M.: 1982, *Astrophys. J.* **254**, 82
Linsky, J.L., Neff, J.E., Brown, A., Gross, B.D., Simon, T., Andrews, A.D., Rodonò, M., Feldman, P.A.: 1988, *Astron. Astrophys.* (in press) (Paper X)
Neff, J.E.: 1987, unpublished Ph. D. thesis, University of Colorado, Boulder
Neff, J.E.: 1988, in *The Impact of Very High S/N Spectroscopy on Stellar Physics, IAU Symp.* **132**, Dordrecht, Kluwer, p. 223
Neff, J.E., Brown, A., Linsky, J.L.: 1989, in *IAU Coll.* **104**, Poster Volume, eds. B.M. Haisch, M. Rodonò, Publ. Catania Astrophys. Obs. (in press)
Neff, J.E., Neff, D.H.: 1987, in *Cool Stars, Stellar Systems, and the Sun*, eds. J.L. Linsky, R.E. Stencel, Springer, Berlin, Heidelberg, New York, p. 531
Neff, J.E., Walter, F.M., Rodonò, M.: 1986, in *New Insights in Astrophysics: Eight Years of Astronomy With IUE*, ESA SP-263, p. 153
Rodonò, M., Byrne, P.B., Neff, J.E., Linsky, J.L., Simon, T., Catalano, S., Cutispoto, G., Doyle, J.G., Andrews, A.D., Gibson, D.M.: 1987, *Astron. Astrophys.* **176**, 267 (Paper III)
Rodonò, M., Cutispoto, G., Pazzani, V., Catalano, S., Byrne, P.B., Doyle, J.G., Butler, C.J., Andrews, A.D., Blanco, C., Marilli, E., Linsky, J.L., Scaltriti, F., Busso, M., Cellino, A., Hopkins, J.L., Okazaki, A., Hayashi, S.S., Zeilik, M., Elston, R., Henson, G., Smith, P., Simon, T.: 1986, *Astron. Astrophys.* **165**, 135 (Paper I)
Simon, T., Linsky, J.L., Shiffer, F.H.: 1980, *Astrophys. J.* **239**, 911
Vogt, S.S., Penrod, G.D.: 1983, *Publ. Astron. Soc. Pacific* **95**, 565
Vogt, S.S., Penrod, G.D., Hatzes, A.P.: 1987, *Astrophys. J.* **321**, 496
Walter, F.M., Gibson, D.M., Brown, A., Carpenter, K.G., Linsky, J.L., Rodonò, M., Eyles, C.: 1984, *Bull. Amer. Astron. Soc.* **16**, 896
Walter, F.M., Neff, J.E., Gibson, D.M., Linsky, J.L., Rodonò, M., Gary, D.E., Butler, C.J.: 1987, *Astron. Astrophys.* **186**, 241 (Paper IV)